THE JOURNAL OF PHYSICAL CHEMISTRY C

Article

Cite This: J. Phys. Chem. C 2018, 122, 6526−6538

pubs.acs.org/JPCC

Lamellar Oxygen-Enriched Graphene Hydrogel with Linking-up Network Porous Structure for High-Performance Supercapacitors

Xiaotong Wang, Yuying Yang,* Quancai Zhang, Xia Yang, and Zhongai Hu*

Key Laboratory of Eco-Environment-Related Polymer Materials of Ministry of Education, Key Laboratory of Polymer Materials of Gansu Province, College of Chemistry and Chemical Engineering, Northwest Normal University, Lanzhou, Gansu 730070, China

Supporting Information

ABSTRACT: Here, we report a lamellar holey oxygen-enriched graphene hydrogel (LGH) consisting of graphene sheets with a large amount of oxygen functional groups and in-plane pores and confirm its excellent supercapacitive performances. LGH is quite different from the traditional graphene hydrogel in terms of both the morphology and porous structure. Importantly, the in-plane pores on the graphene sheets link up the out-of-plane interval between the graphene sheets to form a linking-up network porous structure. The in-plane pores result in more micropores and the additional oxygen functional groups on graphene sheets. The LGH single electrode exhibits an ultrahigh capacitance (337.8 F g^{-1} at 1 A g^{-1}) and excellent rate capability (the specific capacitance at 100 A g^{-1} retains 77% relative to 1 A g^{-1}). The asymmetric supercapacitor is assembled by using the LGH as positive electrode material and the graphene hydrogel that has adsorbed anthraquinone as negative electrode material, respectively. The device exhibits a high energy storage (energy density of 31.5 Wh kg^{-1} along with power density of 0.9 kW kg^{-1}).

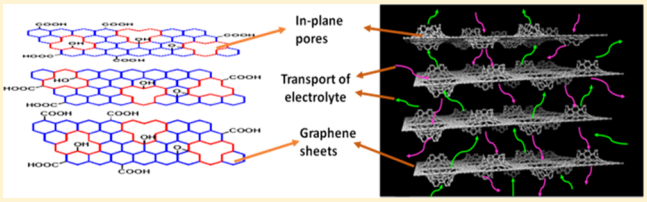

1. INTRODUCTION

Graphene as a single two-dimensional carbonaceous material has been widely used as an electrode material for supercapacitors due to the excellent electrical conductivity, high theoretical surface area, decent flexibility, and outstanding chemical stability.[1−5] But the fact is that in the practical application, the experimental capacitive performance of graphene is far less than the expected value owing to the evident limiting factors. The graphene sheets are easy to agglomerate via the $\pi-\pi$ stacking interaction and van der Waals force. The only outer surface of the agglomerated graphene is accessible to the electrolyte, which leads to the insufficient utilization of active sites.[6−8] To further improve the utilization of the graphene, researchers suggested constructing "spacers" between the graphene sheets. One of the typical examples is the three-dimensional (3D) macropore graphene hydrogel (GH) that is assembled directly from graphene oxide (GO) through the hard template,[9] hydrothermal method,[10,11] and so on. However, the traditional graphene hydrogel seems to have several shortcomings, especially, in the structural parameters. First, the macropores with complicated pore-paths are dominant in the traditional graphene hydrogel, resulting in a limited specific surface area (166 m^2 g^{-1}).[12] Second, the electrolyte ions are not able to pass through pore walls to access the internal-layer graphene in the framework that is assembled from graphene sheets. Third, the lack of oxygen functional groups and hydrophilic properties after further reduction through a hydrothermal reaction limits the capacitive performances of graphene hydrogel.

Recently, the in-plane pores on the graphene sheets are considered an effective strategy to increase the specific surface area and improve the pore structure of the graphene hydrogel.[13−15] Qu et al. reported a graphene nanomesh assembled foam (GMF) with hierarchical pore arrangement by a site-localized nanoparticle-induced etching strategy on the basis of hydrothermally self-assembled graphene architecture. The specific surface area of the resultant GMFs is up to 362 m^2 g^{-1}.[14] Duan et al. reported a holey graphene oxide (HGO) with abundant in-plane nanopores, the specific surface area of ∼430 m^2 g^{-1}, and a pore size distribution in the range of 2−70 nm. The three-dimensional holey graphene framework that derived from the HGO delivered a great gravimetric capacitance of 298 F g^{-1} in organic electrolyte.[16] It is believed that the in-plane pores on graphene sheets have two positive factors: one is that the specific surface area of the graphene hydrogel increases evidently. The other is that the electrolyte ions can directly diffuse into the interior of the graphene hydrogel framework through the in-plane pores on the graphene sheets, leading to an adequate utilization of active sites. It should be noted that the distribution and density of the in-plane pores will influence electric conductivity of the hydrogel. The researchers have been trying to regulate the porosity by using the different pore-forming agents (H_2O_2,[17] KOH,[18] and $KMnO_4$,[19,20] etc.) and controlling the reaction conditions. For instance, Liu et al. prepared a holey reduced graphene oxide (HRGO) with abundant in-plane nanopores by using H_2O_2 as etchant. By optimizing the reaction conditions, pore size distribution of the nanopores ranged from

Received: December 23, 2017
Revised: March 7, 2018
Published: March 7, 2018

DOI: 10.1021/acs.jpcc.7b12644
J. Phys. Chem. C 2018, 122, 6526−6538

0.6 to 5.0 nm. Moreover, the V_{micro}/V_{total} ratio of the obtained HRGO samples increased from 0.083 to 0.167 by prolonging the hydrothermal treatment time. The obtained electrodes exhibited high specific capacitance (251 F g^{-1} at a current density of 1 A g^{-1}) and enhanced rate capability (73% capacitance retention from 1 to 60 A g^{-1}).[21] Yang et al. reported a graphene monolith electrode, in which the zinc chloride ($ZnCl_2$) was used as a pore former to precisely control the density and porosity. The specific surface area was tunable from 370 to over 1000 m^2 g^{-1}. The capacitance of a directly sliced pellet electrode with a thickness of 400 mm reached 150 F cm^{-3} in an ionic liquid electrolyte, and the corresponding symmetrical supercapacitor (SSC) delivered a volumetric energy density of 64.7 Wh L^{-1}.[22]

Besides, the oxygen functional groups on the plane or edge of the graphene layers can strengthen the wettability of the material to improve the accessibility with the aqueous electrolyte, decreasing the charge-transfer resistance between the two-phase boundaries. Meanwhile, Frackowiak et al. considered that the redox reactions of the hydroxyl, carbonyl, and carboxyl groups might be ascribed to the pseudocapacitance behavior.[23] Conway also supported that the quinone or aldehyde groups might possess redox activity, which is responsible for the pseudocapacitive reaction.[24]

It should be noted that capacitive performance of supercapacitors depends on both the positive and negative electrodes. That two electrodes match with each other suitably is essential for achieving high energy density along with large power density. Generally, the positive electrode material where the current response occurs at a positive potential range needs a counterpart in which the current response occurs at a negative potential range. The anthraquinone (AQ) molecule with a reversible Faradaic reaction displays a fast electrochemical response around of −0.2 V in acidic condition.[25] When AQ molecule is confined on the conductive substrates such as graphene via the $\pi-\pi$ interaction, the resultant composite is usually used as a negative electrode material for supercapacitors.[26,27]

Herein, we report a new type of lamellar holey oxygen-enriched graphene hydrogel (LGH), which is quite different from the traditional 3D graphene hydrogel in terms of both the morphology and porous structure. The LGH macroscopically has a long-range ordered structure self-assembled layer by layer, whereas the traditional GH is a three-dimensional framework in which the graphene sheets are randomly configured. After oxide etching with $KMnO_4$, a large number of in-plane pores and additional oxygen functional groups were produced on the graphene sheets. The holey oxygen-enriched graphene sheets were cross-linked into the individual layer during the hydrothermal processes and then the individual layer self-assembled into the macroscopically ordered lamellar structure. The LGH contains abundant in-plane and out-of-plane pores, which leads to a large specific surface area (433.7 m^2 g^{-1}). The in-plane pores on the graphene sheets link up the out-of-plane interval between the graphene sheets to form a hierarchical network porous structure through which the electrolyte ions can directly access to the internal graphene layers in the LGH during the electrochemical processes. As a result, active sites in the LGH can be utilized sufficiently. More importantly, the additional oxygen functional groups are produced around in-plane pores, which contribute enhanced pseudocapacitance to the overall capacitance. Furthermore, LGH has a fast current response at around +0.375 V (vs the saturated calomel electrode (SCE)) in the acidic electrolyte, which is an ideal positive material suitable for supercapacitors. To match with the LGH positive electrode, we used the graphene hydrogel/anthraquinone (GH/AQ) composite as counterpart electrode to assemble asymmetric supercapacitors (ASCs). As a result, the assembled ASC delivers a superior energy density along with high power density. Even at a high power density of 90 kW kg^{-1} (a full charge/discharge only needs 1.7 s), the device preserves energy density of 20 Wh kg^{-1} in aqueous electrolyte solution.

2. EXPERIMENTAL SECTION

2.1. Materials. GO was prepared from pure graphite powder by a modification of the Hummers method.[28,29] Sulfuric acid (98%, H_2SO_4), hydrochloric acid (HCl), acetone, and potassium permanganate ($KMnO_4$) were purchased from Sinopharm Chemical Reagent Corp (China). Anthraquinone was purchased from (AQ, Alfa-Aesar). All of the experiments were carried out using analytical grade chemicals and deionized (DI) water.

2.2. Preparation of Positive Electrode Material. GO (0.16 g) was added into 100 mL of DI water with ultrasonic treatment to form dispersion. A certain amount of $KMnO_4$ was added into the above homogeneous graphene oxide dispersion, and continuous ultrasonic treatment was performed for 1.5 h. Thereafter, the mixture sealed in a 100 mL Teflon-lined autoclave was maintained at 180 °C for 12 h. Then, the autoclave was naturally cooled down to room temperature and the product soaked into HCl (8 M) for 36 h. After being washed repeatedly with DI water and freeze-dried, the LGH materials were obtained. The obtained samples with 0.02, 0.032, and 0.08 g of $KMnO_4$ were marked as LGH-1, 2, and 3, respectively. For comparison, we prepared the graphene hydrogel (GH) by the same procedure in the absence of $KMnO_4$. The GH−MnO_2 was prepared same as LGH-2 and without washing by HCl.

2.3. Preparation of Negative Electrode Material. GH (0.1 g) was soaked in the acetone solution with AQ (the concentration is 1.5 mg mL^{-1}) for 12 h. The final product was washed by acetone several times and dried at 70 °C to obtain GH/AQ negative material.

2.4. Material Characterization. The morphologies of products were characterized by scanning electron microscopy (SEM; Ultra Plus, Germany) and a transmission electron microscope (TEM; JEOL, JEM-2010, Japan). Powder X-ray diffraction (XRD) of materials was implemented on a diffractometer (D/Max-2400) using Cu Kα radiation (λ = 1.5418 Å) operating at 40 kV, 100 mA. Raman spectra was recorded using an inVia Raman spectrometer (Renishaw) with an argon-ion laser (λ = 514 nm). The Brunauer−Emmett−Teller (BET) surface area of the samples was analyzed by nitrogen adsorption in a Micromeritics ASAP 2020 nitrogen adsorption apparatus. Chemical state analyses of samples were performed by X-ray photoelectron spectroscopy (XPS; Escalab 210 system, Germany); the analysis was recorded with a monochromatic Al Kα radiation source (ThermoVG Scientific). Thermogravimetric (TG) analysis was carried out with a PerkinElmer TG/DTA-6300 instrument, and the temperature range is 20−800 °C with a heating rate of 5 °C min^{-1} under the nitrogen atmosphere.

2.5. Electrochemical Measurements. To test the electrochemical performance of the samples in a three-electrode system, the working electrode was prepared by dispersing 85% samples and 15% acetylene black in 0.4 mL of Nafion (0.25 wt %). Then, 6 μL of the above suspension was dropped onto the glassy carbon electrode using a pipette gun and dried at room temperature. Cyclic voltammetry (CV), galvanostatic charge/discharge (GCD), and electrochemical impedance spectroscopy (EIS) were carried out in 1 M H_2SO_4 aqueous solution on a CHI760E

DOI: 10.1021/acs.jpcc.7b12644
J. Phys. Chem. C 2018, 122, 6526−6538

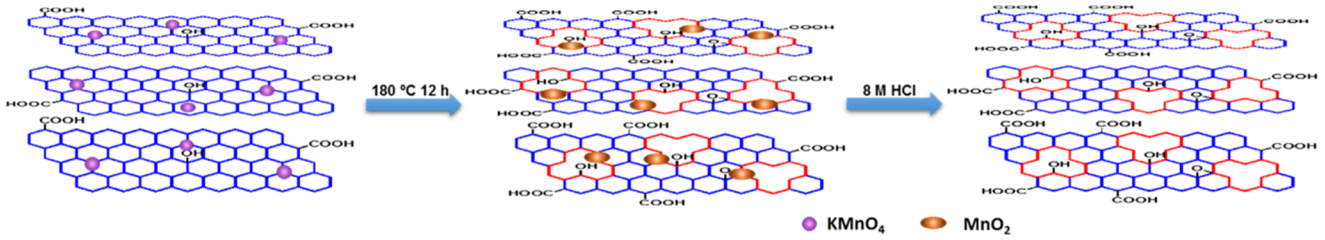

Figure 1. Schematic illustration formation process of LGH electrode material.

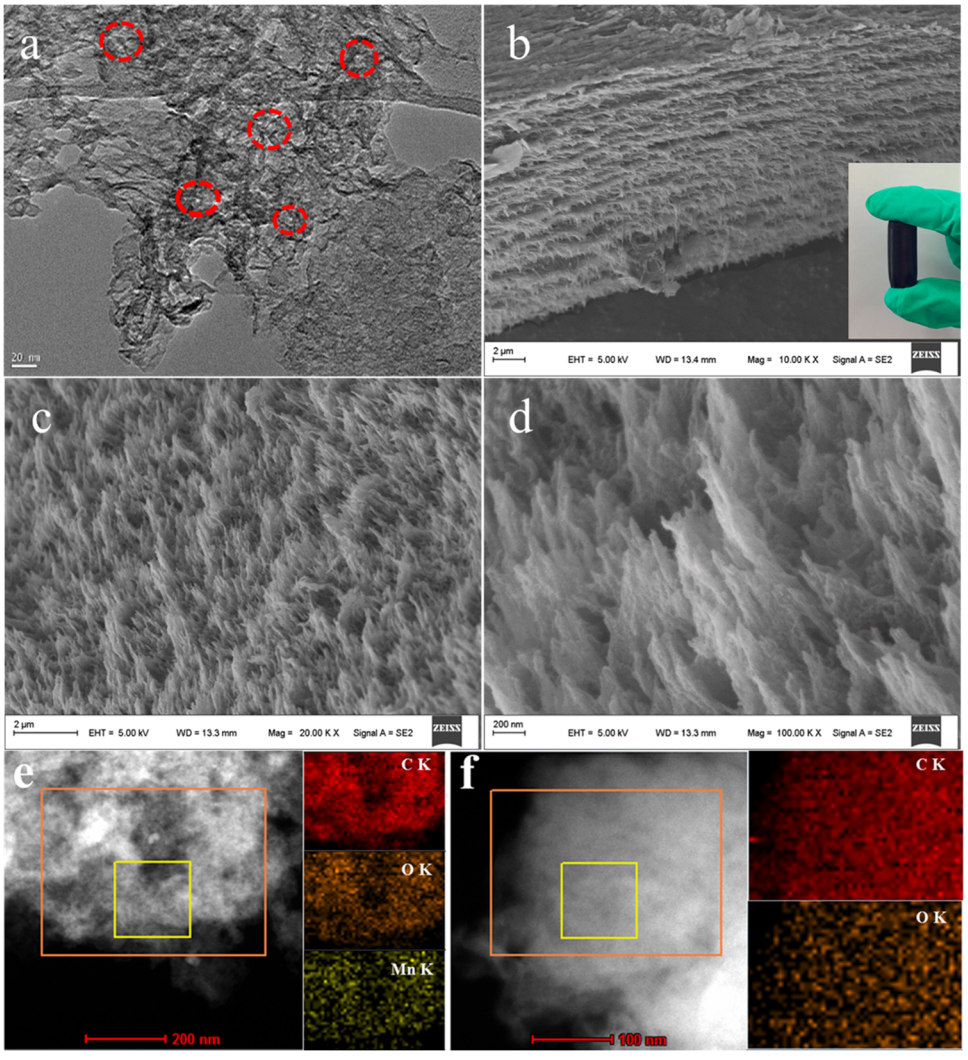

Figure 2. (a) TEM image of LGH-2 (the in-plane pores are marked in the red circles); (b–d) SEM images of LGH-2 at different magnifications, inside (b) is a photograph of LGH-2; (e, f) elemental mapping data TEM images of GH–MnO_2 composite and LGH-2, respectively.

electrochemical working station (Chenghua, Shanghai, China). The carbon rod and saturated calomel electrode were used as the counter electrode and reference electrode, respectively. To evaluate the energy density, an ASC was assembled, in which the LGH-2 and GH/AQ was served as the positive material and negative material, respectively. The charge (Q) on both negative and positive electrodes was balanced on the basis of formula 1a

$$Q = C \times V \times m \tag{1a}$$

where C (F g^{-1}), V (V), and m (g) are specific capacitance, operating potential window, and the mass of the active materials, respectively. The mass loading on both positive and negative electrodes was over 1 mg cm^{-2}. The cycle stability was performed on LANHE test system (Wuhan Electronic Co., Ltd., China).

3. RESULTS AND DISCUSSION

3.1. Positive Materials Characterization. A possible formation process of the material is shown in Figure 1. After adding the $KMnO_4$ aqueous solution into the GO dispersion system, we obtained the reacting system. The carbon atoms would be partly oxidized and consumed to leave behind the carbon vacancies and form in-plane pores on the graphene sheets during the hydrothermal process (reaction 2a), whereas the aqueous permanganate (MnO_4^-) would be converted to the insoluble MnO_2, which might be deposited on the surface of

DOI: 10.1021/acs.jpcc.7b12644
J. Phys. Chem. C 2018, 122, 6526–6538

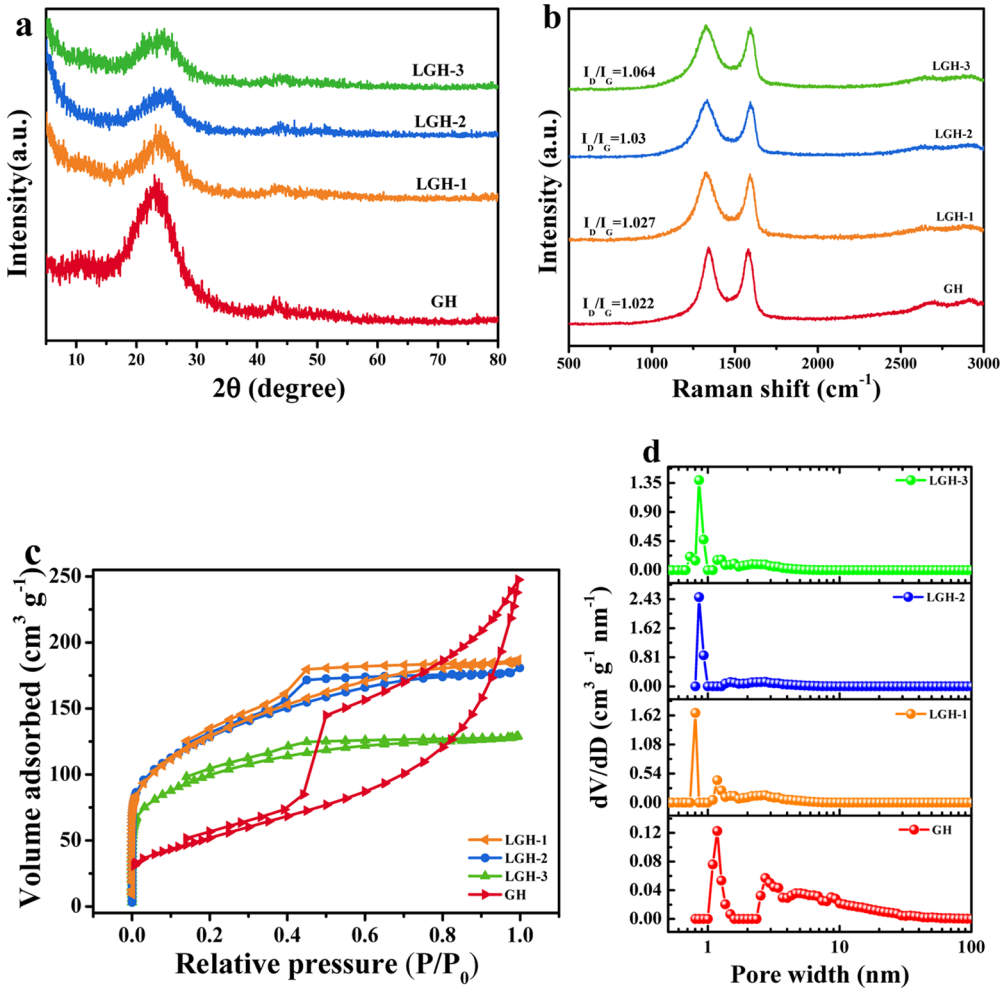

Figure 3. (a) XRD patterns and (b) Raman spectra of GH and LGH-1, 2, and 3 samples; (c) nitrogen adsorption−desorption isotherm and (d) pore size distribution plot of GH and LGH-1, 2, and 3 samples.

graphene sheets.[20,30] Meanwhile, the additional oxygen functional groups would be generated around in-plane pores acting as active sites. The MnO_2 nanoparticles might be connected with these active sites hanging between the graphene layers and then increase the opportunities to form more interconnected layers of the GO.[19] After eliminating the MnO_2 with 8 M HCl, we obtained the LGH materials.

$$4MnO_4^- + 3C + H_2O = 4MnO_2 + CO_3^{2-} + 2HCO_3^- \quad (2a)$$

Figure 2a shows the TEM image of the LGH-2. The LGH-2 consists of the wrinkled and thin multilayered graphene. Furthermore, there are some holes existing on the graphene sheets, which are derived from the chemical activation with $KMnO_4$. The sectional SEM image of the sample is shown in Figure 2b. The macroscopic long-range ordered structure self-assembled layer by layer can be seen clearly, which is defined as lamellar graphene hydrogel. The plane view SEM images of the individual layer are shown in Figure 2c,d, indicating that the layer displays a three-dimensional porous architecture. The observations suggest that the resultant lamellar graphene hydrogel is different from the traditional graphene hydrogel in both morphology and porous structure. This novel lamellar structure might be attributed to the hydrogen bond of the oxygen functional groups and the formation progress of MnO_2 during the oxide-etching reaction. The TEM images of GH−MnO_2 and LGH-2 are shown in Figure S1. It could be observed that the nanoscale MnO_2 particles were anchored on the GH (Figure S1a). After MnO_2 was removed, numerous nanopores were left in the GH (Figure S1b). The elemental mapping analysis images of GH−MnO_2 and LGH-2 are shown in Figure 2e,f, respectively. It is found that C, O, and Mn distribute homogeneously in the GH−MnO_2 composite. After washing with HCl, the Mn element disappeared, indicating that the resulting LGH-2 is only composed of C and O.

The XRD patterns of samples are investigated to evaluate the crystallographic structures (Figure 3a). The XRD patterns of GH and LGH-1, 2, and 3 exhibit broad diffraction peaks located at around $2\theta = 23.6°$, attributing to the (002) plane of graphitic carbon.[31] The intensity of the (002) peak in LGH samples is noticeably weakened and tends to be broad compared to that of the GH. This fact is ascribed to the presence of in-plane pores on the randomly stacked graphene sheets.[32] Raman spectroscopy has been used to investigate the defect structure of graphene materials extensively. There are two broad diffraction peaks at around 1594.2 and 1328.9 cm^{-1}, attributed to the G and D band, respectively. It is generally accepted that the G band is associated with the stretching vibration of the sp^2 carbon atoms in the hexagonal carbon framework, whereas the D band is attributed to the sp^3 hybridized carbon atoms at the edges or defects on graphene basal plane. Therefore, the change of the intensity ratio between the D band and G band (I_D/I_G) can provide an evidence

DOI: 10.1021/acs.jpcc.7b12644
J. Phys. Chem. C 2018, 122, 6526−6538

for the defect formation of graphene sheets.[33,34] As shown in Figure 3b, with the content of $KMnO_4$ growing, the I_D/I_G ratios are 1.022, 1.027, 1.036, and 1.064 for GH and LGH-1, 2, and 3, respectively, suggesting that the increased defects and disorders are attributed to the in-plane pores forming on the graphene sheets.

The porous structure of the samples is further determined by a N_2 adsorption−desorption test (Figure 3c). The isotherms of LGH-1, 2, and 3 belong to type IV. There are steep changes of the adsorption curves at low relative pressure (P/P_0 < 0.1), confirming that there are a large number of micropores. The hysteresis loops observed in the adsorption−desorption isotherm attribute to the capillary condensation at a high relative pressure (P/P_0 is about 0.3−0.9), indicating the existence of mesopores. In the isotherm of GH, an almost vertical tail is present at a P/P_0 of about 0.9−1.0, suggesting that there are macropores in the GH due to the interconnected graphene sheets. Thus, it can be seen that the LGH samples are different from GH in the pore parameters. The former possesses abundant micropores, whereas the latter displays a significant feature of macropores. It is believed that the etching treatment of $KMnO_4$ on the graphene sheets plays a key role in forming micropores. The specific surface area of samples is calculated by the Brunauer−Emmett−Teller (BET) method. As shown in Table 1, the specific surface area of LGH-1, 2, and 3 is 440.8, 433.7, and

Table 1. BET Surface Area, Pore Structure Characterization Parameters of Samples

sample	S_{BET}[a] ($m^2\ g^{-1}$)	D[b] (nm)	V_{total}[c] ($cm^3\ g^{-1}$)	V_{mic}[d]/V_{total} (%)
GH	171.6	8.12	0.345	
LGH-1	440.8	2.63	0.289	11.67
LGH-2	433.7	2.57	0.280	17.14
LGH-3	332.6	2.40	0.199	21.10

[a]Specific surface area determined according to the BET method. [b]Average pore diameter. [c]Total pore volume. [d]Micropores' pore volume.

332.6 $m^2\ g^{-1}$, respectively, which is ~2.5 times larger than that of GH (171.6 $m^2\ g^{-1}$). The increasing specific surface area for LGH samples might be owing to the uniformly distributed in-plane pores on graphene sheets. The hierarchical porous configuration of the samples is also confirmed by the pore size distribution plot, as shown in Figure 3d. The micropores of LGH-1, 2, and 3 are centered at around 0.80, 0.86, and 0.86 nm, respectively. The meso/macropores have continuous distribution within the range of 2−100 nm. By adding the $KMnO_4$, the content of macropores decreases greatly. It is noticed that LGH-2 shows a denser distribution in pore sizes centered below 1 nm, indicating its relatively higher porosity. The micropore volumes of LGH-1, 2, and 3 are up to 11.67, 17.14, and 21.10% of the total pore volume, respectively.[35]

It is generally considered that the oxygen functional groups are present on the plane and edge of graphene sheets. For holey graphene, oxygen functional groups are also considered to be around in-plane pores on graphene sheets.[36,37] To further investigate the surface composition, the XPS was performed. The XPS full spectra of samples are shown in Figure 4. Only the primary C 1s and O 1s peaks appear at around 285.1 and 533.3 eV, confirming that the samples contain none other impurities. The oxygen contents are 8.93, 15.02, 16.73, and 17.74% for GH, LGH-1, 2, and 3 samples, respectively (Table 2). The oxygen contents increase gradually with the etching degree, indicating

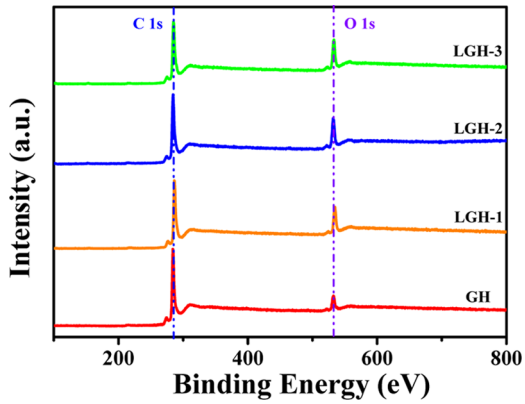

Figure 4. XPS spectrum survey scans of GH, LGH-1, 2, and 3 samples.

Table 2. Summary of Elemental Composition of Samples

samples	GH	LGH-1	LGH-2	LGH-3
C (%)	91.07	84.98	83.27	82.26
O (%)	8.93	15.02	16.73	17.74

that the oxide etching could enhance the level of oxygen content effectively. This phenomenon corresponds to the regular change of the micropore contents, so we speculate that the oxygen content is related with the formation of micropores and the oxygen functional groups might be existing on the edges of micropores.

As shown in Figure 5a, three peaks were fitted by the deconvolution of the C 1s spectra. They correspond to graphitic carbon (284.7 eV), C−O (285.8 eV), and C═O/C(O)O (288.5 eV), respectively.[38] The relative quantity of each species is listed in Figure 6a and Table 3. The amount of graphitic carbon components decreases from 75.85% (GH) to 61.18% (LGH-1), 55.2% (LGH-2), and 57.54% (LGH-3), implying that the sp^2 carbon atoms in graphene are further reduced by etching. Meanwhile, the summations of C−O and C═O/C(O)O components of LGH are increased obviously compared to those of GH and the LGH-2 owns the highest content. The high-resolution O 1s spectra of samples are revealed in Figure 5b. The peaks of three types of oxygen functionalities are C═O/C(O)O (531.9 eV), C−O−C (532.7 eV), and −OH (533.6 eV) groups.[39] The reversible redox reactions are believed to take place between the hydroxyl and carboxyl groups during the electrochemistry process.[40] From Figure 6b and Table 3, we further calculated the total contents of the electroactive oxygen functional groups (C═O/C(O)O and −OH groups), which are equal to 43.09 (GH), 60.81 (LGH-1), 74.59 (LGH-2), and 64.73% (LGH-3), respectively. The oxygen functional groups with electrochemical activity could contribute the pseudocapacitance to the overall capacitance during the electrochemical process.

To evaluate the electrochemical performances of the samples for supercapacitors, we measured the CV curves in a three-electrode system in the electrolyte of 1 M H_2SO_4 solution. As shown in Figure 7a, the CV curves of GH and LGH-1, 2, and 3 were compared at a potential window of 0−1 V, with the scan rate at 10 mV s^{-1}. All of the CV curves show a similar rectangular shape, with a pair of redox peaks. Comparatively, the background currents of LGH are larger than those of GH, suggesting a significant enhanced double layer charge storage capability of LGH. This result attributes to the higher specific surface area of LGH. The LGH-2 has the largest background current of LGH

DOI: 10.1021/acs.jpcc.7b12644
J. Phys. Chem. C 2018, 122, 6526−6538

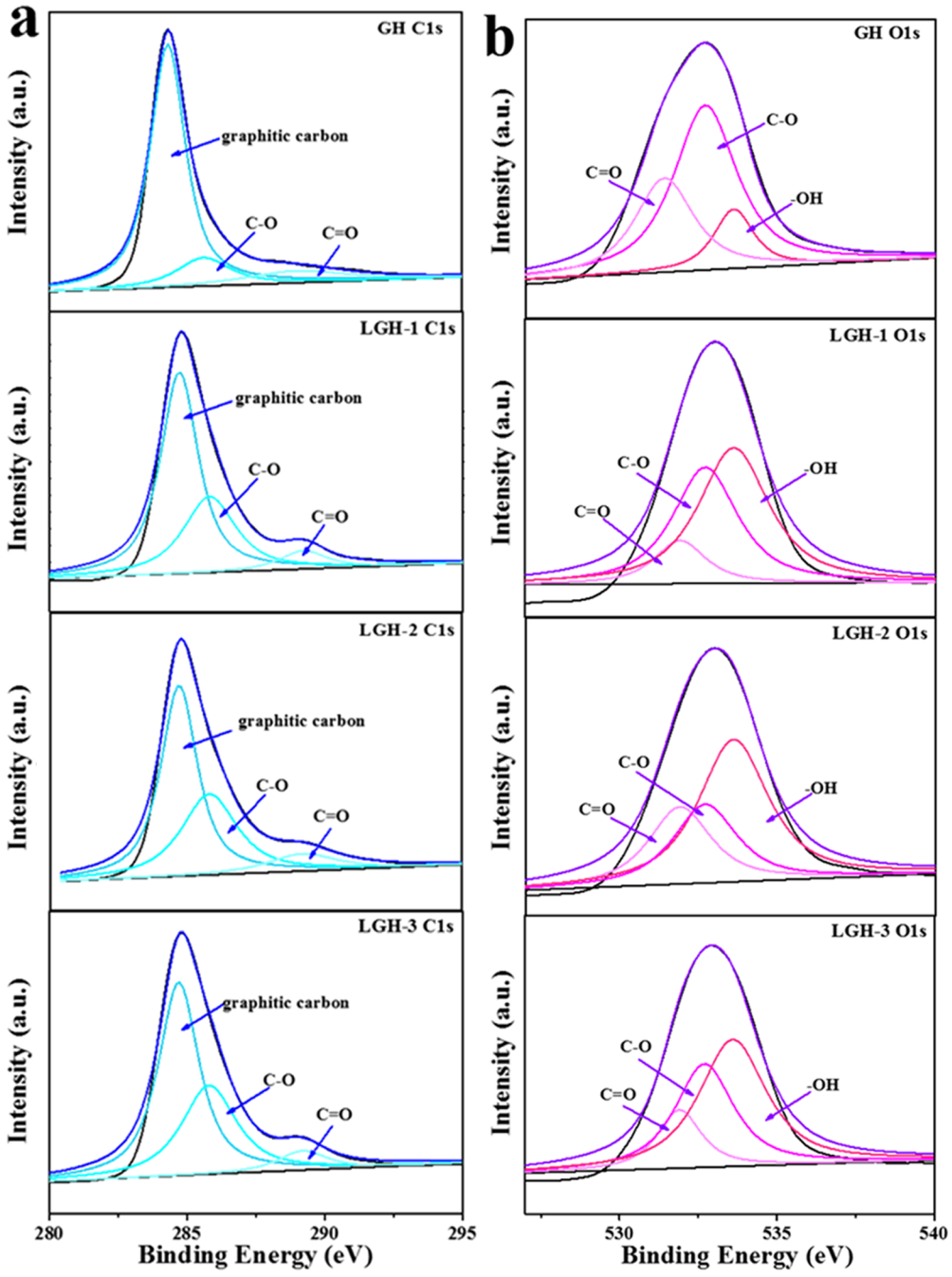

Figure 5. XPS spectra of C 1s region (a) and O 1s region (b) of GH, LGH-1, 2, and 3 samples.

Table 3. Fitted Results (atom %) of C 1s and O 1s XPS Spectra for Samples

	C 1s			O 1s		
assignment	graphitic carbon (284.7 eV)	C−O (285.8 eV)	C═O/C(O)O (289.2 eV)	C═O/C(O)O (531.4 eV)	C−O−C (532.7 eV)	O−H (533.6 eV)
GH	75.85	13.44	10.71	30.21	56.91	12.88
LGH-1	61.18	31.82	7.00	11.55	39.19	49.26
LGH-2	55.20	35.50	9.30	24.34	25.41	50.25
LGH-3	57.54	35.60	6.86	15.02	35.27	49.71

samples, which might be relative to a sufficient contact area between the electrode materials and the electrolyte. It is reported that the reversible redox reaction of the oxygen-containing functional groups occurs at around +0.4 V.[40,41] Compared with LGH-1 and LGH-3, there is a relatively expanded integral area of the CV curve and strong redox peak for LGH-2 at about +0.375 V, which could attribute to the relatively more oxygen functional groups with electrochemical activity and more complete electrical conductivity. Thus, it is an effective way to improve the performance of the carbon materials by oxide-etching

DOI: 10.1021/acs.jpcc.7b12644
J. Phys. Chem. C 2018, 122, 6526−6538

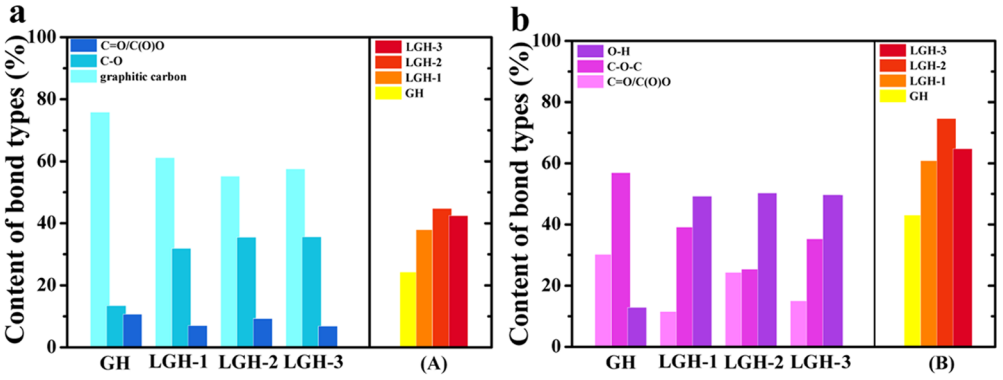

Figure 6. Relative surface contents of carbon and oxygen species obtained by fitting the C 1s XPS; the C 1s (a) and O 1s (b) of GH and LGH-1, 2, and 3 ((A) is the summation of C═O/C(O)O and C−O; (B) is the summation of O−H and C═O/C(O)O).

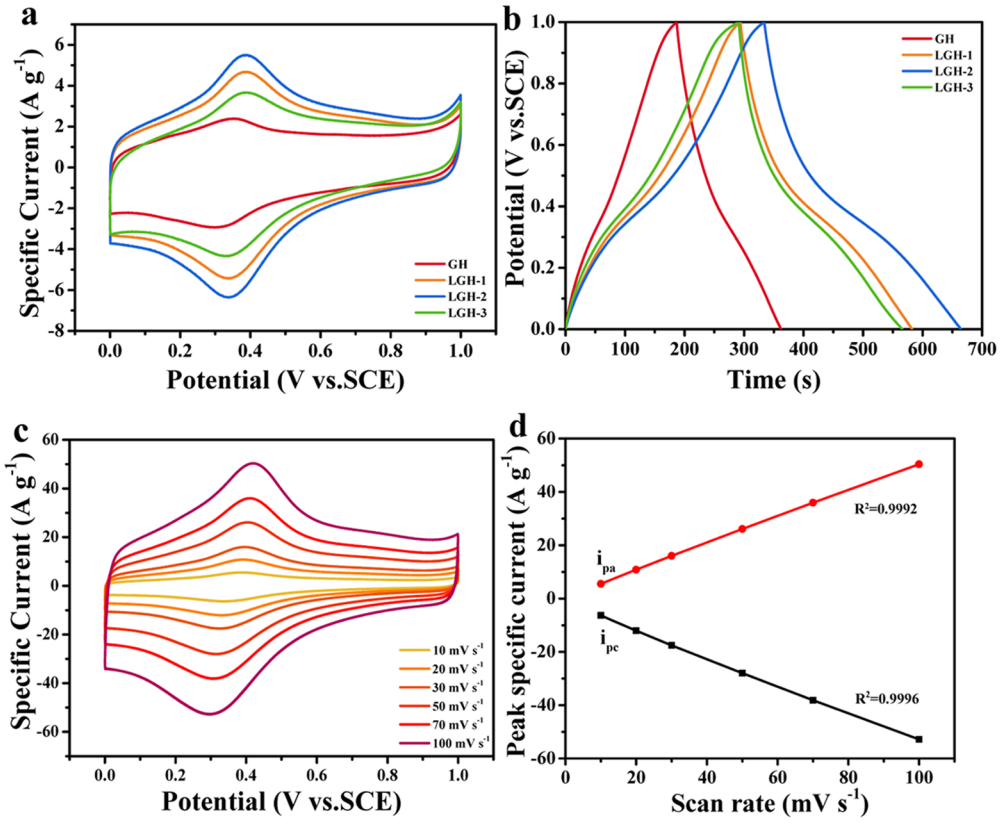

Figure 7. (a) CV and (b) GCD curves of GH and LGH-1, 2, and 3 at a scan rate of 10 mV s^{-1} and current density of 1 A g^{-1} in 1 M H_2SO_4, respectively; (c) CV curves of LGH-2 at different scan rates; (d) the relationship between the peak current of LGH-2 and the scan rate.

treatment that increases the oxygen functional groups with electrochemical activity. The oxygen functional group reaction may be accounted as follows (reaction 1), which can be regarded as two electronic responses[40,42]

$$>C^{-}OH \underset{H^+ + e^-}{\rightleftharpoons} >C{=}O \overset{H_2O}{\underset{H^+ + e^-}{\rightleftharpoons}} >COOH \qquad \text{(Reaction 2)}$$

The energy storage performances of samples are further tested with the galvanostatic charge/discharge experiments. As shown in Figure 7b, the galvanostatic curves of GH and LGH-1, 2, and 3 exhibit nonlinear shapes, indicating the presence of pseudocapacitive reactions, which is consistent with the results of CV. The specific capacitance C (F g^{-1}) of samples was calculated on the basis of the galvanostatic charge/discharge curves according to following formula 3

$$C = \frac{I \cdot \Delta t}{\Delta V \cdot m} \qquad (3)$$

where I (A) is the discharge current, Δt (s) is the discharge time, ΔV (V) is the voltage interval of discharge, and m (g) is the mass of active material. The specific capacitances of the GH and LGH-1, 2, and 3 electrodes are 175.3, 274.7, 337.8, and 288.6 F g^{-1} at 1 A g^{-1}, respectively. The highest specific capacitance of LGH-2 could attribute to the maximum content of electroactive oxygen functional groups and the rational distribution between the special surface area and pore size.

Figures 7c and S2a show the CVs of LGH-2 electrode at different rates. All of the curves display a shape similar to that of a pair of the redox peak; the integral area of CV curves and the peak current increase gradually with the increase of the scan rate, but

DOI: 10.1021/acs.jpcc.7b12644
J. Phys. Chem. C 2018, 122, 6526−6538

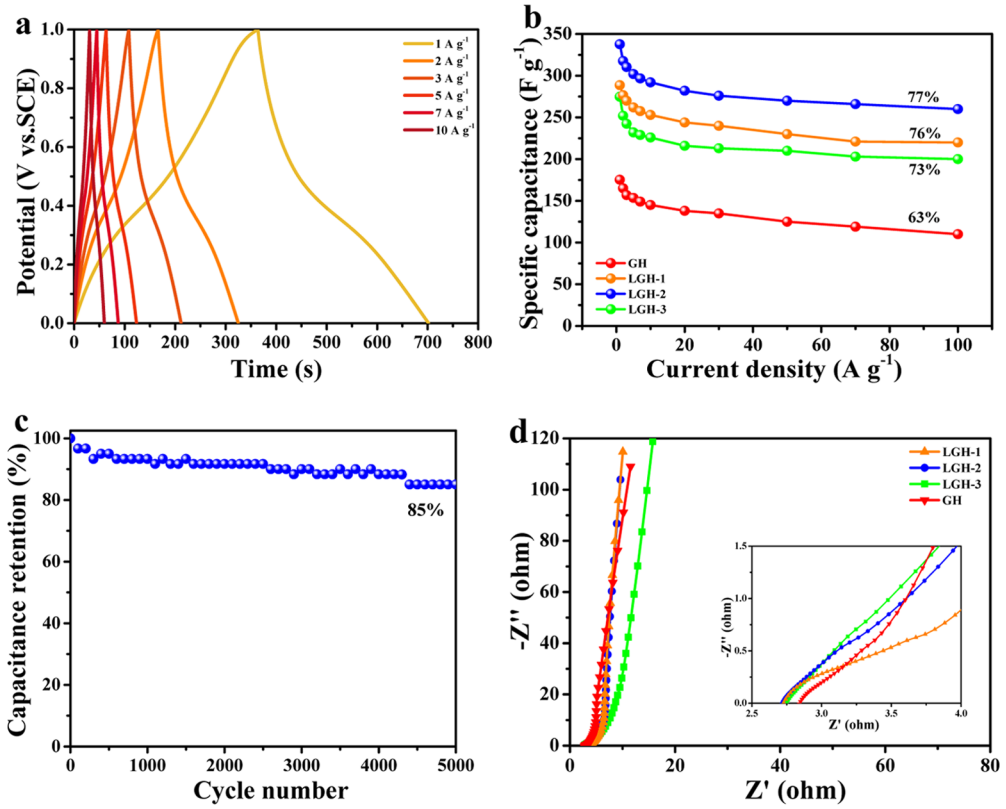

Figure 8. (a) GCD curves of LGH-2 at different current densities; (b) specific capacitances of GH and LGH-1, 2, and 3 at various current densities; (c) the cycling stability of LGH-2 at 5 A g^{-1} in 1 M H_2SO_4; (d) Nyquist plots of GH and LGH-1, 2, and 3; the inset shows the close-up view of the high-frequency region.

the shape is maintained when the scan rate increased to 100 mV s^{-1}. This suggests a low polarization and fast current response during electrode processes. To investigate the dynamic characteristics of the LGH-2 electrode material, the relation between the peaks' current (i) and applied scan rate (v) was analyzed, according to the formula 4[43]

$$i = av^b \tag{4}$$

where a and b are regulatory factors. When the redox reaction is limited by semi-infinite diffusion, the current response varies with the square root of the scan rate ($b = 1/2$); limited by surface control, the current varies directly with the scan rate ($b = 1$). As shown in Figure 7d, a linear relationship is observed between i and v for the redox peaks, (the oxidation and reduction coefficient are R_O^2 = 0.999 and R_R^2 = 0.999, respectively), indicating that the electrochemical reaction process of LGH-2 is similar to a capacitive process and not limited by concentration diffusion.

Furthermore, GCD curves of LGH-2 are measured at various current densities from 1 to 10 A g^{-1} (Figure 8a) and 10 to 100 A g^{-1} (Figure S2b) at the potential window from 0 to 1 V. As shown in Figure 8a, the GCD curves reveal a favorable symmetry with an obvious charge/discharge platform, indicating that such an electrode possesses excellent electrochemical reversibility. The correlation between the specific capacitance and the various current densities for different electrodes is illustrated in Figure 8b. When the current density increased to 100 A g^{-1}, the specific capacitance still remains at 260 F g^{-1}, with about 77.1% capacitance retention relative to 1 A g^{-1} (337 F g^{-1}) for LGH-2. This value is significantly higher than that of LGH-1 (76%), LGH-3 (73%), and GH (63%). The excellent rate capability of LGH-2 could attribute to the complete electrical network, the linking-up porous structure, and the enrichment of electroactive oxygen. This porous structure leads to a shortcut for electrolyte effectively infiltrating into the electrode materials and decreases the resistance of the electrolyte transport. The oxygen functional groups could improve the wettability of the graphene materials, resulting in an easier accessibility of electrolyte to the materials. The cycle stability of the LGH-2 electrode was evaluated by a continuous charge/discharge cycling test between 0 and 1 V (vs SCE) at 5 A g^{-1}. As shown in Figure 8c, the capacitance of LGH-2 can be retained at 85% after 5000 cycles, indicating an excellent electrochemical stability.

The electrochemical impedance spectrum (EIS) is measured to investigate the kinetic features of the electrodes. Figure 8d shows the typical Nyquist plots of GH and LGH-1, 2, and 3 in 1 M H_2SO_4, and the bias potential is 0.2 V. There are two major features in the high- and low-frequency regions that are consequent to the different resistance phenomena during the electrochemical process.[44] In the high-frequency region (Figure 8d inside), we can observe that the samples show the inconspicuous semicircle, which attributed to a lower charge-transfer resistance of the electrochemical reaction. The intercept along the x axis corresponds to the equivalent series resistance, which includes the electrolyte resistance, intrinsic resistance of the active material, and contact resistance between the active material and current collector interface. The LGH-2 electrode exhibits the smallest intercept value, which could attribute to the oxygen on the surface of the graphene sheets improving the wettability and decrease the contact resistance between the electrolyte and electrode materials. Moreover, the LGH-2 shows a more vertical line in low frequency than others, indicating that

DOI: 10.1021/acs.jpcc.7b12644
J. Phys. Chem. C 2018, 122, 6526−6538

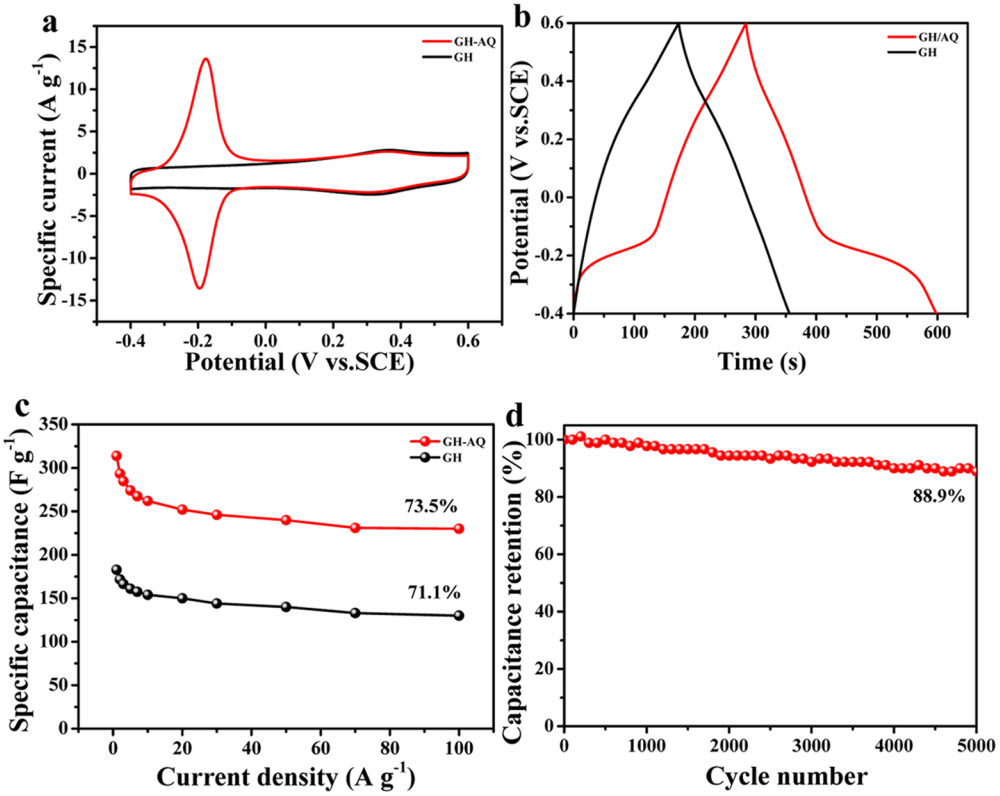

Figure 9. (a) CV curves and (b) GCD curves of GH and GH/AQ at a scan rate of 10 mV s^{-1} and current density of 1 A g^{-1}, respectively; (c) specific capacitances of GH and GH/AQ at various current densities; (d) the cycling stability of GH/AQ at 5 A g^{-1} in 1 M H_2SO_4.

the LGH-2 possesses lesser diffusive resistance between with the electrolyte and electrode material. This phenomenon indicated that the LGH-2 maintains the conductive network completely even though it has the least graphite carbon and its in-plane pores increase the contact area between the LGH electrodes and electrolyte. Simultaneously, the oxygen-containing groups could improve the hydrophilicity of the electrode materials to promote the electrolyte ions diffusing into the electrode materials.

3.2. Negative Materials Characterization. To match the capacitive behaviors of a positive electrode, graphene hydrogel/anthraquinone composite material (GH/AQ) was prepared as a negative electrode. The morphologies of the GH and GH/AQ are imaged by SEM (Figure S3a,b). It is shown that the GH and GH/AQ have the same structure with the interconnected 3D macropores that consist of the ultrathin graphene nanosheets. It is confirmed that the noncovalent modification does not affect morphology of the GH. Figure S3c is Raman spectra of GH and GH/AQ. The I_D/I_G value of GH/AQ is 0.989, which decreases obviously compared to that of the GH (I_D/I_G about 1.022). It could attribute to the improvement of graphitic fields or just an overlap with C=C vibrations of AQ in the spectrum, which further confirms that the noncovalent functionalization strategy can effectively preserve the conjugated structure of graphene.[45]

For estimating the content of AQ molecule in GH/AQ, the thermogravimetric analysis (TGA) was tested under the nitrogen atmosphere. Owing to the sublimation, the AQ starts to lose the weight in the temperature range of 200−275 °C (Figure S3d). Compared with the bare AQ, weight loss of AQ in GH/AQ composite occurs at higher temperatures, which attribute to the layered structure of graphene impeding the sublimation of the AQ.[27] The content of AQ in the GH/AQ composite can be calculated to about 15.5%.

The electrochemical performances of GH and GH/AQ are estimated in the potential range from −0.4 to 0.6 V. The CV curves are shown in Figure 9a; the background currents of two samples almost coincide, proving that the original capacitance performance of the GH is still maintained after modifying with AQ molecules. Compared with the GH, the CV curve of GH/AQ has a pair of symmetrical redox peaks at around −0.175 V, obviously indicating that the redox reaction of GH/AQ composite is a rapid and reversible process. The aromatic rings of AQ molecules are parallel with the conjugated carbon skeleton of the GH through the $\pi-\pi$ stacking interaction. This structure can protect the conductive structure of the original graphene and provide a shorter distance to promote the communication between the graphene and electrochemical active sites. The conversion of AQ to 9, 10-dihydroxyanthracene (AQH_2) in acidic aqueous solution is a two-electron and two-proton process; the corresponding redox reaction is shown below (reaction 2)[46,47]

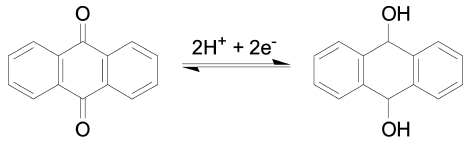

(Reaction 3)

We also test the CV of GH/AQ in different scan rates (Figure S4a). The curves keep the original shapes without obvious distortion when the scan rate increases from 10 to 100 mV s^{-1}, suggesting an excellent capacitance behavior. The response of the anodic (i_{pa}) and cathodic (i_{pc}) peak specific current with the scan rates has been measured. It can be seen from Figure S4b, the current varies directly with the scan rates, suggesting that the redox reaction of the GH/AQ is similar to a capacitive process.

DOI: 10.1021/acs.jpcc.7b12644
J. Phys. Chem. C 2018, 122, 6526−6538

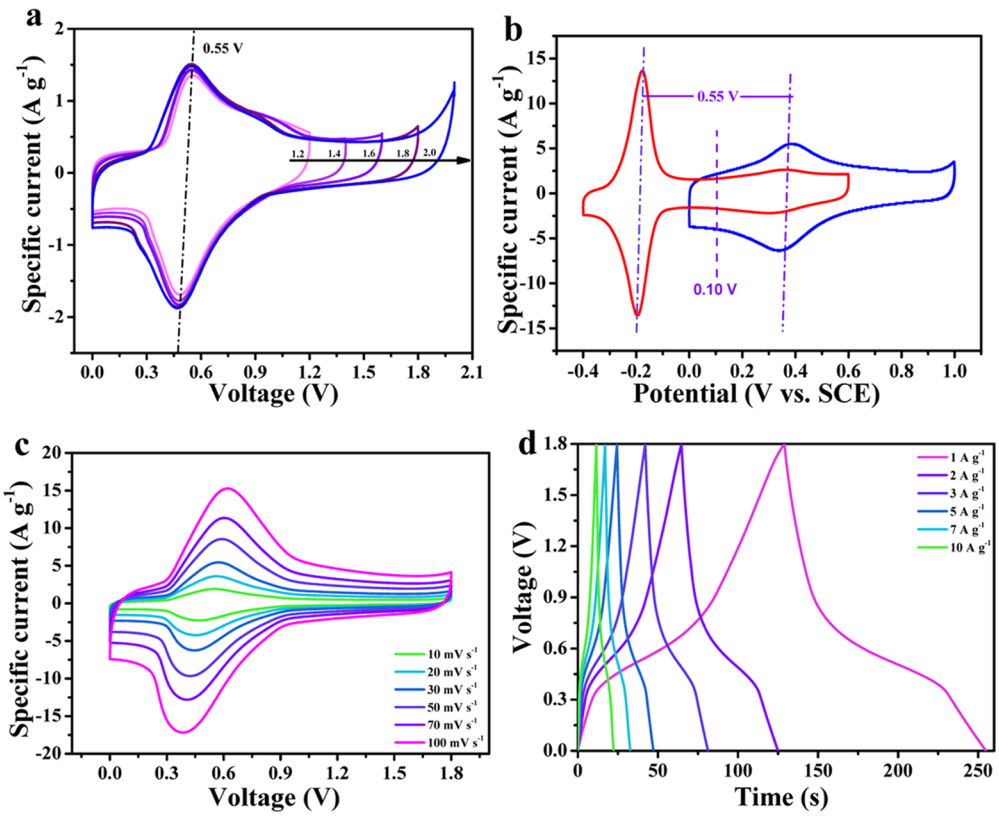

Figure 10. (a) CV of the two-electrode system for GH/AQ//LGH-2 ASC with different cell voltages at a scan rate of 10 mV s^{-1} in 1 M H_2SO_4; (b) Comparative CV of GH/AQ and LGH-2 electrodes in a three-electrode system at a scan rate of 10 mV s^{-1}; (c) CV curves of GH/AQ//LGH-2 ASC at different scan rates; (d) GCD of GH/AQ//LGH-2 ASC at various current densities.

The GCD curves of GH and GH/AQ at 1 A g^{-1} are displayed in Figure 9b. The GCD curve of GH exhibits a highly symmetrical isosceles triangle shape. However, for the GH/AQ composite, there is a charge/discharge plateau, which is well in agreement with the CV analysis. The GCD curves of GH/AQ maintain symmetry perfectly with the current density increasing to 10 A g^{-1} (Figure S4c). The specific capacitances of GH and GH/AQ are calculated to be 182.8 and 313.1 F g^{-1} at the current density of 1 A g^{-1}, respectively. This remarkable capacitance improvement could attribute to the additional pseudocapacitance of AQ and the strong positive synergistic effects between AQ and GH.

The specific capacitance of GH/AQ with different current densities is shown in Figure 9c. The specific capacitance at 100 A g^{-1} can still be maintained at 73.5% of the one at 1 A g^{-1}, which is larger than the rate capability of GH (71%). The AQ molecules tend to be parallel and close to the sp^2 network of the graphene by the $\pi-\pi$ stacking interaction, leading to a fast charge transfer of AQ on the GH with a low-charge-transfer resistance. After 5000 cycles, the capacitance retention of GH/AQ is 88.9% at 5 A g^{-1} (Figure 9d). The outstanding cycle performance of GH/AQ indicates that a repeatable stable energy storage process can be maintained during the multiple cycles.

Nyquist plots of GH/AQ and GH electrodes are presented in Figure S3d. In the high-frequency region, the impedance plot of GH/AQ shows the inconspicuous semicircle that is because of the reversible redox couples (AQ/AQH_2) on the surface of graphene sheets. As shown in the inset of Figure S4d, the intercept of GH/AQ is a little higher than that of GH, indicating that the electrical conductivity of the GH/AQ electrode system is relatively smaller, which could attribute to the poor electronic conductivity of AQ. The impedance plot along with the imaginary axis of the GH/AQ and GH is almost vertical, reflecting the great capacitive behavior.

3.3. Performances of the GH/AQ//LGH-2 ASC. To evaluate the realistic performances of materials, an asymmetric supercapacitor (ASC) was assembled by using LGH-2 and GH/AQ as the positive and negative electrodes, respectively. Figure 10a shows the CV curves of GH/AQ//LGH-2 ASC at a scan rate of 10 mV s^{-1} in 1 M H_2SO_4. The GH/AQ//LGH-2 ASC demonstrates an ideal capacitive behavior without obvious oxygen evolution curves, even at the cell voltage as large as 1.8 V. In addition, it is notable that there is a pair of distinguished and reversible redox peaks appearing in the CV curve at about 0.55 V. Compared with the CV curves of positive and negative electrode materials in a three-electrode configuration, we can detect that the deviation between LGH-2 and GH/AQ redox peak positions also equals 0.55 V. This phenomenon can be explained as follows: when the ASC charges in the voltage range from 0 to 0.55 V, the positive and negative electrodes of the ASC will, respectively, achieve an electrochemical state at the corresponding potential in the three-electrode system; that is, the beginning voltage (0 V) for the ASC is equivalent to 0.1 V in the three-electrode system because the electrodes have the same electrochemical state. When the charging voltage of the ASC increases from 0 to 0.55 V, the corresponding potential value of the positive electrode shifts positively from 0.1 to 0.375 V in the three-electrode system, whereas the corresponding potential of the negative electrode shifts negatively from 0.1 to −0.175 V, which corresponds to the individual redox peaks (Figure 10b). When the oxide current of the positive electrode and reduced current of the negative electrode reach their maximum value

DOI: 10.1021/acs.jpcc.7b12644
J. Phys. Chem. C 2018, 122, 6526−6538

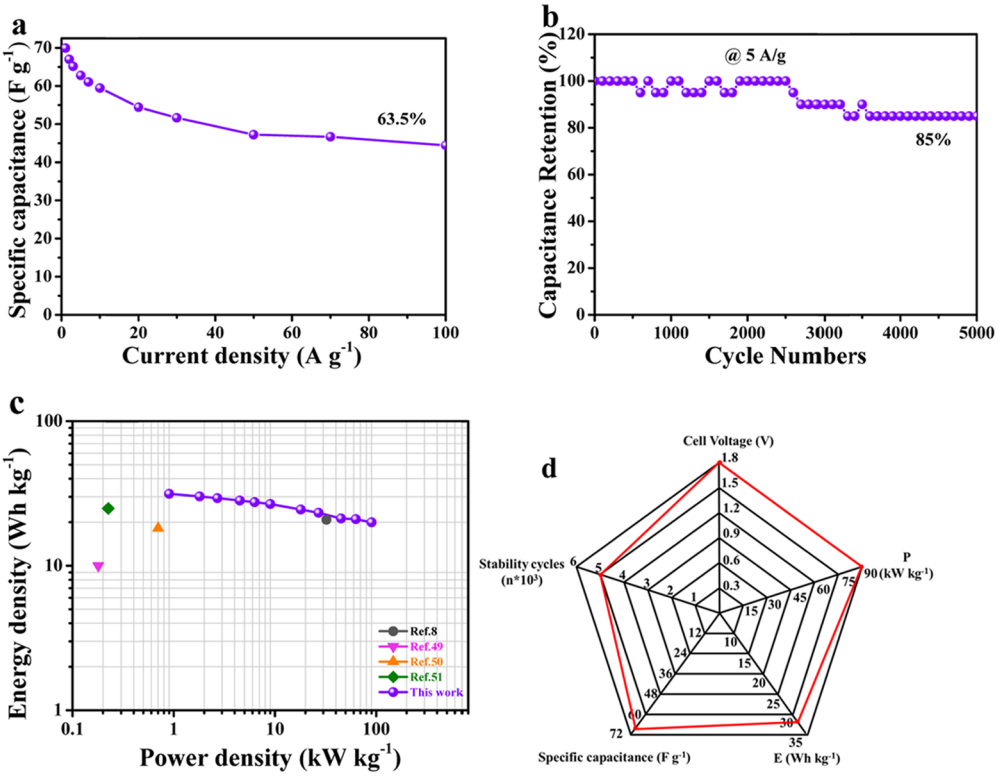

Figure 11. (a) Specific capacitance of GH/AQ//LGH-2 ASC at various current densities; cycling stability and Ragone plot of the ACS in (b) and (c), respectively; (d) radar plots of the ASC, the red curve is generated from the GH/AQ//LGH-2 ASC using 1 M H_2SO_4 electrolyte.

simultaneously, the charging peak appears on the CV curve in the two-electrode system. Conversely, the backward reversible process takes place during the discharging for ASC. Figures 10c and S5a show the CV curves of GH/AQ//LGH-2 ASC at scan rates from 10 to 100 mV s^{-1} and 100 to 1000 mV s^{-1}, respectively. The shape of CV curves remains almost unchanged with the increasing scan rate, suggesting a fast diffusion of electrolyte ions into the electrode materials. The GCD curves of the GH/AQ//LGH-2 ASC at different current densities from 1 to 10 A g^{-1} and 10 to 100 A g^{-1} are shown in Figures 10d and S5b, respectively, in which a plateau at around 0.55 V is consistent with the CV curves. Additionally, all curves are almost symmetrical, indicating an excellent electrochemical reversibility.

The relationship between current density and specific capacitance is demonstrated in Figure 11a. The specific capacitance of GH/AQ//LGH-2 ASC is up to 69.8 F g^{-1} at 1 A g^{-1} and still retains 63.5% even at 100 A g^{-1}. Moreover, the cycling stability of GH/AQ//LGH-2 ASC is evaluated by repeating the GCD test at a current density of 5 A g^{-1} (Figure 11b). After 5000 cycles, the GH/AQ//LGH-2 ASC exhibits electrochemical stability with about 85% retention of the initial specific capacitance, indicating a remarkable long-term stability of the ASC.

Energy and power densities are important parameters to describe the practical application of supercapacitors. We evaluated the energy and power densities of the GH/AQ//LGH-2 ASC from the galvanostatic charge/discharge curves at various current density using eqs 5 and 6

$$E = \frac{0.5C(\Delta V)^2}{3.6} \tag{5}$$

$$P = \frac{E}{t} \tag{6}$$

where E is energy density (Wh kg^{-1}) and P is power density (kW kg^{-1}) of the supercapacitor. C (F g^{-1}) is the specific capacitance of the ASC, ΔV (V) is voltage window, and t (s) is discharge time.[48] The Ragone plot relative to the corresponding energy and power densities of the GH/AQ//LGH-2 ASC is shown in Figure 11c. It can be observed that the GH/AQ//LGH-2 ASC delivers a high energy density of 31.5 Wh kg^{-1} along with the power density of 0.9 kW kg^{-1} and preserved a good energy density of 20 Wh kg^{-1} even at power density of 90 kW kg^{-1}. On comparing with the other works in Figure 11c, it is indicated that the GH/AQ//LGH-2 ASC is probably superior to many reported symmetric or asymmetric supercapacitors in aqueous electrolyte, such as the ASC fabricated with activated microwave expanded graphite oxide (aMEGO) and the aMEGO deposited by manganese dioxide,[8] the ASC with anthraquinone and dihydroxybenzene-modified carbon fabric electrodes,[49] SSC with graphene hydrogels functionalized by alizarin,[50] the ASC based on cobalt hydroxide/graphene, and polypyrrole/graphene electrodes.[51] The radar plot which is shown in Figure 11d assesses the electrochemical performance of GH/AQ//LGH-2 ASC systematically.

The excellent energy storage performance of the GH/AQ//LGH-2 ASC can be interpreted as follows: First, for the positive electrode material, the linking-up porous structure with a high specific surface area curtails the diffusion distance of electrolyte ions. Simultaneously, the oxygen functional groups on the graphene sheets could improve the surface wettability and contribute pseudocapacitance to the overall capacitance. Second, for the negative electrode material, the AQ molecules absorbed on the GH/AQ can afford a multielectron redox reaction and

DOI: 10.1021/acs.jpcc.7b12644
J. Phys. Chem. C 2018, 122, 6526−6538

respond with the change of potential immediately. Third, the LGH-2 and GH/AQ as the positive and negative electrodes, respectively, have a self-matching behavior. Finally, the redox reactions of LGH-2 and GH/AQ are limited by surface control, which provides a kinetic condition for matching positive and negative half reactions.

4. CONCLUSIONS

In summary, we prepared a lamellar oxygen-enriched graphene hydrogel with a linking-up network porous structure. $KMnO_4$ plays an important role in the formation of the LGH. As an etchant, $KMnO_4$ creates the abundance of oxygen functional groups and in-plane pores on the graphene sheets through the reaction with carbon atoms. The in-plane pores on the graphene sheets lead to large specific surface area of the sample. The content of electroactive oxygen functional groups on the graphene sheets is a key factor that enhances electrochemical performance in terms of capacitance and rate capability. The LGH as a positive electrode can match with the GH/AQ to assemble an ASC. The ASC exhibits an excellent energy storage performance with the ultrahigh energy density of 31.5 Wh kg^{-1} along with power density of 0.9 kW kg^{-1}. This all-carbon and green electrode material exhibits a promising application prospect.

■ ASSOCIATED CONTENT

Supporting Information

The Supporting Information is available free of charge on the ACS Publications website at DOI: 10.1021/acs.jpcc.7b12644.

TEM images of LGH-MnO_2 and LGH-2; CV and GCD curves of LGH; SEM, Raman spectra and TGA of GH/AQ; CV and GCD curves, the relationship between the peak current and scan rates of CV curves; Nyquist plots of GH/AQ, CV, and GCD curves of GH/AQ//LGH-2 ASC (PDF)

■ AUTHOR INFORMATION

Corresponding Author

*E-mail: zhongai@nwnu.edu.cn; y_yuying@163.com. Tel: +86 931 7973255. Fax: +86 931 8859764.

ORCID

Zhongai Hu: 0000-0003-3933-7252

Notes

The authors declare no competing financial interest.

■ ACKNOWLEDGMENTS

The authors gratefully acknowledge the financial support offered by the National Natural Science Foundation of China (20963009, 21163017, 21563027, and 21773187).

■ REFERENCES

(1) Liu, C.; Yu, Z.; Neff, D.; Zhamu, A.; Jang, B. Z. Graphene-Based Supercapacitor with an Ultrahigh Energy Density. *Nano Lett.* **2010**, *10*, 4863−4868.

(2) Simon, P.; Gogotsi, Y. Capacitive Energy Storage in Nanostructured Carbon−Electrolyte Systems. *Acc. Chem. Res.* **2013**, *46*, 1094−1103.

(3) Geim, A. K.; Novoselov, K. S. The Rise of Graphene. *Nat. Mater.* **2007**, *6*, 183−191.

(4) Peng, Y.-Y.; Liu, Y.-M.; Chang, J.-K.; Wu, C.-H.; Ger, M.-D.; Pu, N.-W.; Chang, C.-L. A Facile Approach to Produce Holey Graphene and Its Application in Supercapacitors. *Carbon* **2015**, *81*, 347−356.

(5) Novoselov, K. S.; Fal'ko, V. I.; Colombo, L.; Gellert, P. R.; Schwab, M. G.; Kim, K. A Roadmap for Graphene. *Nature* **2012**, *490*, 192−200.

(6) Han, S.; Wu, D.; Li, S.; Zhang, F.; Feng, X. Porous Graphene Materials for Advanced Electrochemical Energy Storage and Conversion Devices. *Adv. Mater.* **2014**, *26*, 849−864.

(7) Mukherjee, R.; Thomas, A. V.; Krishnamurthy, A.; Koratkar, N. Photothermally Reduced Graphene as High-power Anodes for Lithium-ion Batteries. *ACS Nano* **2012**, *6*, 7867−7878.

(8) Zhao, X.; Zhang, L.; Murali, S.; Stoller, M. D.; Zhang, Q.; Zhu, Y.; Ruoff, R. S. Incorporation of Manganese Dioxide within Ultraporous Activated Graphene for High-Performance Electrochemical Capacitors. *ACS Nano* **2012**, *6*, 5404−5412.

(9) Li, Y.; Chen, J.; Huang, L.; Li, C.; Hong, J.-D.; Shi, G. Highly Compressible Macroporous Graphene Monoliths via an Improved Hydrothermal Process. *Adv. Mater.* **2014**, *26*, 4789−4793.

(10) Jiang, L.; Fan, Z. Design of Advanced Porous Graphene Materials: from Graphene Nanomesh to 3D Architectures. *Nanoscale* **2014**, *6*, 1922−1945.

(11) Xu, Y.; Sheng, K.; Li, C.; Shi, G. Self-Assembled Graphene Hydrogel via a One-step Hydrothermal Process. *ACS Nano* **2010**, *4*, 4324−4330.

(12) Zhang, L.; Shi, G. Preparation of Highly Conductive Graphene Hydrogels for Fabricating Supercapacitors with High Rate Capability. *J. Phys. Chem. C* **2011**, *115*, 17206−17212.

(13) Chen, S.; Duan, J.; Tang, Y.; Qiao, S. Z. Hybrid Hydrogels of Porous Graphene and Nickel Hydroxide as Advanced Supercapacitor Materials. *Chem. − Eur. J.* **2013**, *19*, 7118−7124.

(14) Zhao, Y.; Hu, C.; Song, L.; Wang, L.; Shi, G.; Dai, L.; Qu, L. Functional Graphene Nanomesh Foam. *Energy Environ. Sci.* **2014**, *7*, 1913−1918.

(15) Chen, S.; Duan, J.; Jaroniec, M.; Qiao, S. Z. Hierarchically Porous Graphene-based Hybrid Electrodes with Excellent Electrochemical Performance. *J. Mater. Chem. A* **2013**, *1*, 9409−9413.

(16) Xu, Y.; Chen, C.-Y.; Zhao, Z.; Lin, Z.; Lee, C.; Xu, X.; Wang, C.; Huang, Y.; Shakir, M. I.; Duan, X. Solution Processable Holey Graphene Oxide and Its Derived Macrostructures for High-Performance Supercapacitors. *Nano Lett.* **2015**, *15*, 4605−4610.

(17) Xu, Y.; Lin, Z.; Zhong, X.; Huang, X.; Weiss, N. O.; Huang, Y.; Duan, X. Holey Graphene Frameworks for Highly Efficient Capacitive Energy Storage. *Nat. Commun.* **2014**, *5*, No. 4554.

(18) Jiang, Z.-j.; Jiang, Z.; Chen, W. The Role of Holes in Improving the Performance of Nitrogen-doped Holey Graphene as an Active Electrode Material for Supercapacitor and Oxygen Reduction Reaction. *J. Power Sources* **2014**, *251*, 55−65.

(19) Lv, W.; Tao, Y.; Ni, W.; Zhou, Z.; Su, F.-Y.; Chen, X.-C.; Jin, F.-M.; Yang, Q.-H. One-pot Self-assembly of Three-Dimensional Graphene Macroassemblies with Porous Core and Layered Shell. *J. Mater. Chem.* **2011**, *21*, 12352−12357.

(20) Fan, Z.; Zhao, Q.; Li, T.; Yan, J.; Ren, Y.; Feng, J.; Wei, T. Easy Synthesis of Porous Graphene Nanosheets and Their Use in Supercapacitors. *Carbon* **2012**, *50*, 1699−1703.

(21) Bai, Y.; Yang, X.; He, Y.; Zhang, J.; Kang, L.; Xu, H.; Shi, F.; Lei, Z.; Liu, Z.-H. Formation Process of Holey Graphene and Its Assembled Binder-Free Film Electrode with High Volumetric Capacitance. *Electrochim. Acta* **2016**, *187*, 543−551.

(22) Li, H.; Tao, Y.; Zheng, X.; Luo, J.; Kang, F.; Cheng, H.-M.; Yang, Q.-H. Ultra-Thick Graphene Bulk Supercapacitor Electrodes for Compact Energy Storage. *Energy Environ. Sci.* **2016**, *9*, 3135−3142.

(23) Frackowiak, E.; Béguin, F. Carbon Materials for the Electrochemical Storage of Energy in Capacitors. *Carbon* **2001**, *39*, 937−950.

(24) Conway, B. E. *Electrochemical Supercapacitors: Scientific Fundamentals and Technological Applications*; Kluwer Academic/Plenum Publishers: New York, 1999.

(25) An, N.; An, Y.; Hu, Z.; Zhang, Y.; Yang, Y.; Lei, Z. Green and All-carbon Asymmetric Supercapacitor Based on Polyaniline Nanotubes and Anthraquinone Functionalized Porous Nitrogen-doped Carbon Nanotubes with High Energy Storage Performance. *RSC Adv.* **2015**, *5*, 63624−63633.

DOI: 10.1021/acs.jpcc.7b12644
J. Phys. Chem. C 2018, 122, 6526−6538

(26) Guo, B.; Hu, Z.; An, Y.; An, N.; Jia, P.; Zhang, Y.; Yang, Y.; Li, Z. Nitrogen-doped Heterostructure Carbon Functionalized by Electroactive Organic Molecules for Asymmetric Supercapacitors with High Energy Density. *RSC Adv.* **2016**, *6*, 40602−40614.
(27) An, N.; Zhang, F.; Hu, Z.; Li, Z.; Li, L.; Yang, Y.; Guo, B.; Lei, Z. Non-covalently Functionalizing Graphene Framework by Anthraquinone for High-rate Electrochemical Energy Storage. *RSC Adv.* **2015**, *5*, 23942−23951.
(28) Hummers, W. S., Jr.; Offeman, R. E. Preparation of Graphitic Oxide. *J. Am. Chem. Soc.* **1958**, *80*, 1339.
(29) Kovtyukhova, N. I.; Ollivier, P. J.; Martin, B. R.; Mallouk, T. E.; Chizhik, S. A.; Buzameva, E. V.; Goorchinskiy, A. D. Layer-by-Layer Assembly of Ultrathin Composite Films from Micron-Sized Graphite Oxide Sheets and Polycations. *Chem. Mater.* **1999**, *11*, 771−778.
(30) Jin, X.; Zhou, W.; Zhang, S.; Chen, G. Z. Nanoscale Microelectrochemical Cells on Carbon Nanotubes. *Small* **2007**, *3*, 1513−1517.
(31) Nethravathi, C.; Rajamathi, M. Chemically Modified Graphene Sheets Produced by The Solvothermal Reduction of Colloidal Dispersions of Graphite Oxide. *Carbon* **2008**, *46*, 1994−1998.
(32) Wang, Q.; Yan, J.; Wang, Y.; Wei, T.; Zhang, M.; Jing, X.; Fan, Z. Three-Dimensional Flower-like and Hierarchical Porous Carbon Materials as High-rate Performance Electrodes for Supercapacitors. *Carbon* **2014**, *67*, 119−127.
(33) Ferrari, A. C.; Basko, D. M. Raman Spectroscopy as a Versatile Tool for Studying the Properties of Graphene. *Nat. Nanotechnol.* **2013**, *8*, 235−246.
(34) Hernandez, Y.; Nicolosi, V.; Lotya, M.; Blighe, F. M.; Sun, Z. S.; De, S.; McGovern, I. T.; Holland, B.; Byrne, M.; Gun'ko, Y. K.; et al. High-yield Production of Graphene by Liquid-Phase Exfoliation of Graphite. *Nat. Nanotechnol.* **2008**, *3*, 563−568.
(35) An, Y.; Yang, Y.; Hu, Z.; Guo, B.; Wang, X.; Yang, X.; Zhang, Q.; Wu, H. High-performance Symmetric Supercapacitors Based on Carbon Nanosheets Framework with Graphene Hydrogel Architecture Derived from Cellulose Acetate. *J. Power Sources* **2017**, *337*, 45−53.
(36) Szabó, T.; Berkesi, O.; Forgó, P.; Josepovits, K.; Sanakis, Y.; Petridis, D.; Dékány, J. Evolution of Surface Functional Groups in a Series of Progressively Oxidized Graphite Oxides. *Chem. Mater.* **2006**, *18*, 2740−2749.
(37) Tojo, T.; Sakural, K.; Muramatsu, H.; Hayashi, T.; Yang, K.-S.; Jung, Y. C.; Yang, C.-M.; Endo, M.; Kim, Y. A. Electrochemical Role of Oxygen Containing Functional Groups on Activated Carbon Electrode. *RSC Adv.* **2014**, *4*, 62678−62683.
(38) Chen, C.-M.; Zhang, Q.; Yang, M.-G.; Huang, C.-H.; Yang, Y.-G.; Wang, M.-Z. Structural Evolution During Annealing of Thermally Reduced Graphene Nanosheets for Application in Supercapacitors. *Carbon* **2012**, *50*, 3572−3584.
(39) Oda, H.; Yamashita, A.; Minoura, S.; Okamoto, M.; Morimoto, T. Modification of the Oxygen-Containing Functional Group on Activated Carbon Fiber in Electrodes of an Electric Double-layer Capacitor. *J. Power Sources* **2006**, *158*, 1510−1516.
(40) Fan, X.; Lu, Y.; Xu, H.; Kong, X.; Wang, J. Reversible Redox Reaction on the Oxygen-Containing Functional Groups of an Electrochemically Modified Graphite Electrode for the Pseudocapacitance. *J. Mater. Chem.* **2011**, *21*, 18753−18760.
(41) Sullivan, M. G.; Kötz, R.; Haas, O. Thick Active Layers of Electrochemically Modified Glassy Carbon. Electrochemical Impedance Studies. *J. Electrochem. Soc.* **2000**, *147*, 308−317.
(42) Phattharasupakun, N.; Wutthiprom, J.; Suktha, P.; Iamprasertun, P.; Chanlek, N.; Shepherd, C.; Hadzifejzovic, E.; Moloney, M. G.; Foord, J. S.; Sawangphruk, M. High-performance Supercapacitors of Carboxylate-Modified Hollow Carbon Nanospheres Coated on Flexible Carbon Fibre Paper: Effects of Oxygen-Containing Group Contents, Electrolytes and Operating Temperature. *Electrochim. Acta* **2017**, *238*, 64−73.
(43) Augustyn, V.; Simon, P.; Dunn, B. Pseudocapacitive Oxide Materials for High-rate Electrochemical Energy Storage. *Energy Environ. Sci.* **2014**, *7*, 1597−1614.
(44) Huang, S.; Wang, J.; Pan, Z.; Zhu, J.; Shen, P. K. Ultrahigh Capacity and Superior Stability of Three-Dimensional Porous Graphene Networks Containing In Situ Grown Carbon Nanotube Clusters as Anode Material for Lithium-Ion Batteries. *J. Mater. Chem. A* **2017**, *5*, 7595−7602.
(45) Chen, X.; Wang, H.; Yi, H.; Wang, X.; Yan, X.; Guo, Z. Anthraquinone on Porous Carbon Nanotubes with Improved Supercapacitor Performance. *J. Phys. Chem. C* **2014**, *118*, 8262−8270.
(46) Tomai, T.; Mitani, S.; Komatsu, D.; Kawaguchi, Y.; Honma, I. Metal-free Aqueous Redox Capacitor via Proton Rocking-chair System in an Organic-based Couple. *Sci. Rep.* **2014**, *4*, No. 3591.
(47) Sarapuu, A.; Vaik, K.; Schiffrin, D. J.; Tammeveski, K. Electrochemical Reduction of Oxygen on Anthraquinone-Modified Glassy Carbon Electrodes in Alkaline Solution. *J. Electroanal. Chem.* **2003**, *541*, 23−29.
(48) Yan, J.; Liu, J.; Fan, Z.; Wei, T.; Zhang, L. High-performance Supercapacitor Electrodes Based on Highly Corrugated Graphene Sheets. *Carbon* **2012**, *50*, 2179−2188.
(49) Algharaibeh, Z.; Pickup, P. G. An Asymmetric Supercapacitor with Anthraquinone and Dihydroxybenzene Modified Carbon Fabric Electrodes. *Electrochem. Commun.* **2011**, *13*, 147−149.
(50) An, N.; An, Y.; Hu, Z.; Guo, B.; Yang, Y.; Lei, Z. Graphene Hydrogels Functionalized Non-covalently by Alizarin: an Ideal Electrode Materials for Symmetric Supercapacitor. *J. Mater. Chem. A* **2015**, *3*, 22239−22246.
(51) Cai, X.; Lim, S. H.; Poh, C. K.; Lai, L.; Lin, J.; Shen, Z. High-performance Asymmetric Pseudocapacitor Cell Based on Cobalt Hydroxide/Graphene and Polypyrrole/Graphene Electrodes. *J. Power Sources* **2015**, *275*, 298−304.

DOI: 10.1021/acs.jpcc.7b12644
J. Phys. Chem. C 2018, 122, 6526−6538